Supplementary Information

Dean M. Sweeney, Bolton Tran, and Bryan R. Goldsmith*

Department of Chemical Engineering, University of Michigan, Ann Arbor, MI

E-mail: bgoldsm@umich.edu

Dopant Segregation and Aggregation Modeling in JDFTx

All DFT calculations for the segregation and aggregation studies were performed using the Joint Density Functional Theory Software (JDFTx) with the Revised Perdew-Burke-Ernzerhof functional. A plane wave energy cutoff of 544 eV was used for valence electron expansion, while the core electrons were accounted for using projected augmented wave potentials. Spin-polarized calculations were done for Ni_1Cu only. Each surface was modeled using a $3 \times 3 \times 5$ supercell with the top 4 layers able to relax (along with adsorbates) and the bottom layer fixed in its lattice coordinates. The Brillouin zone was sampled with a $4 \times 4 \times 1$ Monkhorst–Pack k-point grid. Periodic images in the z-direction were separated by a vacuum layer of 15 Å to minimize periodic interactions. Forces were converged to <0.01 eV/Å.

A surface atom in the Cu host metal (computed lattice constant: 3.70 Å) was replaced by a dopant atom to simulate the SAA structure. For aggregation studies, an adjacent Cu atom on the surface layer was replaced by a dopant. For segregation studies, a Cu atom in the third layer was replaced by a dopant atom to simulate the dopant in the subsurface while the surface layer was pure Cu. This methodology was benchmarked with the results of Darby et al., as shown in Figure S1.[1]

For computing grand free energies, we used the CANDLE implicit solvation model to

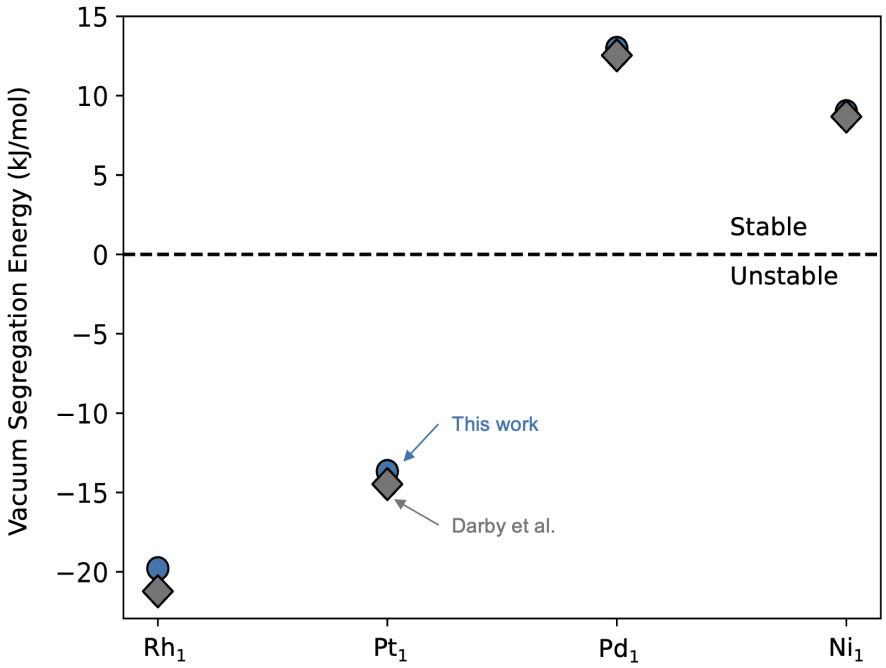

Figure S1: Dopant segregation energies for X_1Cu SAAs calculated in vacuum compared to the work of Darby et al.[1]

simulate solvent and ion effects. To simulate an applied potential, we set the electronic Fermi energy (equal to the electrochemical potential of an electron, μ_e) to the target potential, which was converted to the SHE scale via $U_{\text{SHE}} = \frac{-\mu_e - \phi_{\text{ref}}}{e}$. In this work, $\phi_{\text{ref}} = 4.66$ eV, as calibrated to the CANDLE implicit solvation model.

Segregation energies and aggregation energies for bare surface slabs (without adsorbates present) are calculated via eqs. (S1) and (S2) and shown in Table S1. In these equations Φ_{Cu}, Φ_{SAA}, Φ_{dimer}, and Φ_{bulk} are the grand free energies of the surface with just Cu, a single dopant (SAA), clustered dopant atoms (dimer), or when the dopant is in the subsurface (bulk). The partial charges for all dopants are shown in Figure S2.

$$\Delta\Phi_{\text{seg}} = \Phi_{\text{bulk}} - \Phi_{\text{SAA}} \tag{S1}$$

$$\Delta\Phi_{\text{agg}} = \Phi_{\text{dimer}} + \Phi_{\text{Cu}} - 2\Phi_{\text{SAA}} \tag{S2}$$

Table S1: Segregation and aggregation energies computed from explicit GC-DFT for surfaces without adsorbates present (units: kJ/mol)

	$\Delta\Phi_{seg}(-0.114\ V)$	$\Delta\Phi_{seg}(-0.714\ V)$	$\Delta\Phi_{agg}(-0.114\ V)$	$\Delta\Phi_{agg}(-0.714\ V)$
Ti_1Cu	–2.58	–18.61	12.93	12.35
Ni_1Cu	–20.12	–19.22	–1.23	–1.37
Nb_1Cu	–21.52	–29.07	–59.95	–57.07
Ru_1Cu	–32.62	–30.11	–35.87	–36.40
Rh_1Cu	–13.70	–11.75	4.75	4.26
Pd_1Cu	13.27	14.35	10.89	10.72
Pt_1Cu	9.90	12.84	13.13	13.00
Au_1Cu	50.95	53.05	13.81	14.09

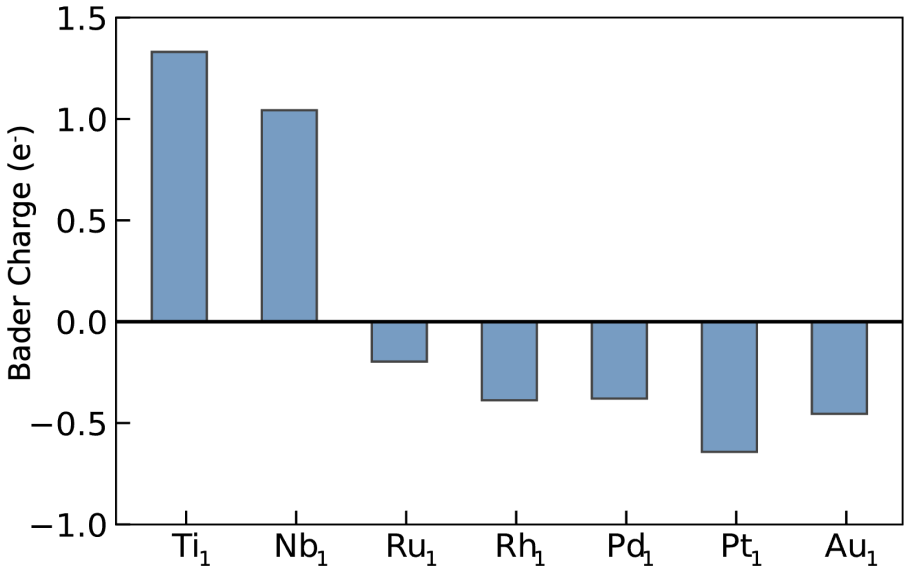

Figure S2: Bader charge analysis of the dopant atom in the X_1Cu surface at -0.114 V vs SHE as computed in JDFTx.

Segregation energies and aggregation energies, when H* and NO_3* are present, are calculated via eqs. (S3) and (S4) as shown in Tables S2 and S3. In these equations, $\Delta\Phi^{(A^*)}_{\text{ads, Cu}}$, $\Delta\Phi^{(A^*)}_{\text{ads, SAA}}$, and $\Delta\Phi^{(A^*)}_{\text{ads, Dimer}}$ represent the adsorption free energies of an adsorbate, A*, on a pure Cu site, a SAA site, and a dimer site. Note that when taking the difference in adsorption energies for a given adsorbate, the reference states for each adsorption energy will cancel out.

$$\Delta\Phi^{(A^*)}_{\text{seg}} = \Delta\Phi_{\text{seg}} + (\Delta\Phi^{(A^*)}_{\text{ads, Cu}} - \Delta\Phi^{(A^*)}_{\text{ads, SAA}}) \tag{S3}$$

$$\Delta\Phi^{(A^*)}_{\text{agg}} = \Delta\Phi_{\text{agg}} + (\Delta\Phi^{(A^*)}_{\text{ads, Dimer}} - \Delta\Phi^{(A^*)}_{\text{ads, SAA}}) \tag{S4}$$

Table S2: Segregation and aggregation energies computed from explicit GC-DFT when H* is adsorbed on dopant X_1 in X_1Cu (units: kJ/mol)

	$\Delta\Phi^{H^*}_{\text{seg}}(-0.114\text{ V})$	$\Delta\Phi^{H^*}_{\text{seg}}(-0.714\text{ V})$	$\Delta\Phi^{H^*}_{\text{agg}}(-0.114\text{ V})$	$\Delta\Phi^{H^*}_{\text{agg}}(-0.714\text{ V})$
Ti_1Cu	9.02	–0.52	–6.30	–14.35
Ni_1Cu	–1.90	–0.89	–14.32	–13.44
Nb_1Cu	–1.90	–6.12	–68.16	–78.83
Ru_1Cu	–2.32	0.46	–28.13	–29.06
Rh_1Cu	7.19	9.62	–1.69	–2.35
Pd_1Cu	15.41	17.21	7.02	6.64
Pt_1Cu	16.66	19.23	9.25	9.36
Au_1Cu	30.55	31.93	29.64	30.28

Table S3: Segregation and aggregation energies computed from explicit GC-DFT when NO_3^* is adsorbed on dopant X_1 in X_1Cu (units: kJ/mol)

	$\Delta\Phi_{seg}^{NO_3^*}(-0.114\ V)$	$\Delta\Phi_{seg}^{NO_3^*}(-0.714\ V)$	$\Delta\Phi_{agg}^{NO_3^*}(-0.114\ V)$	$\Delta\Phi_{agg}^{NO_3^*}(-0.714\ V)$
Ti_1Cu	79.63	75.81	–60.90	–73.48
Ni_1Cu	–4.06	–5.06	–13.95	–11.86
Nb_1Cu	75.45	69.75	–133.32	–141.30
Ru_1Cu	-4.05	–3.00	-58.80	–53.16
Rh_1Cu	–5.44	–3.40	–2.77	-0.24
Pd_1Cu	4.88	8.95	17.62	14.17
Pt_1Cu	–9.87	–5.83	31.06	-
Au_1Cu	25.32	-	-	-

The adsorption configurations of NO_3^* on the SAA sites as optimized from GC-DFT is shown in Figure S3. The configuration of NO_3^* on Ti_1Cu and Nb_1Cu indicates that the molecule interacts strongly with the Ti_1 and Nb_1 sites over Cu. Conversely, the configuration of NO_3^* on Au_1Cu indicates that it interacts weakly with the Au_1 sites.

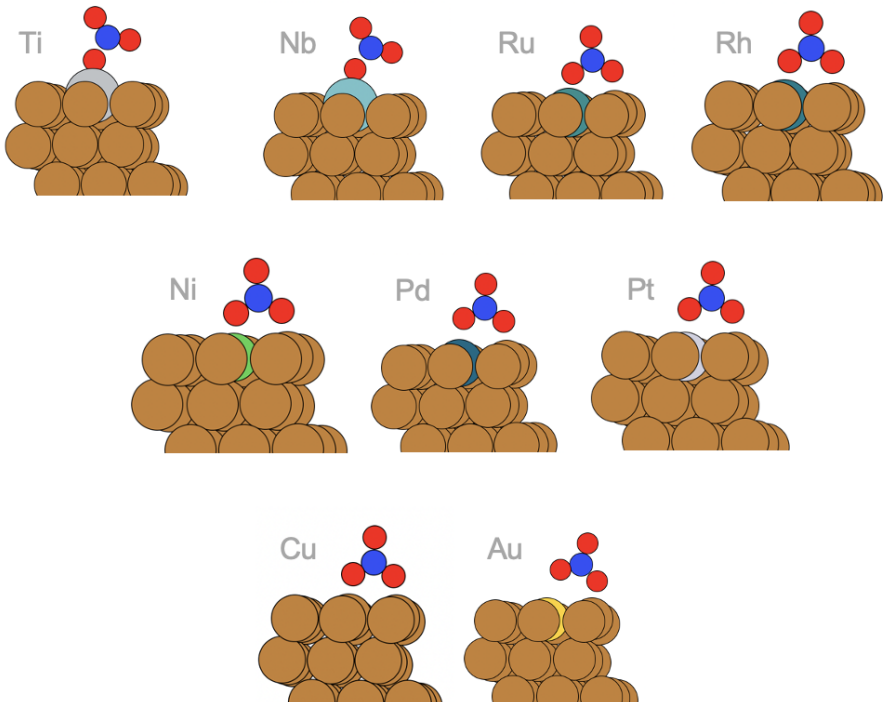

Figure S3: Adsorption configurations for NO_3^* optimized with GC-DFT for all SAAs at -0.714 V vs SHE. Each surface is labeled by the dopant atom in grey.

Potential Dependence of Nitrate Adsorption and Dissociation

Thermodynamic Cycle for Nitrate Adsorption

DFT cannot accurately calculate the free energy of an aqueous-phase anion, which is necessary for the intuitive reaction pathway for NO_3^- adsorption (ΔG_{14}). Therefore, we use a new thermodynamic cycle to avoid the calculation of aqueous NO_3^-.

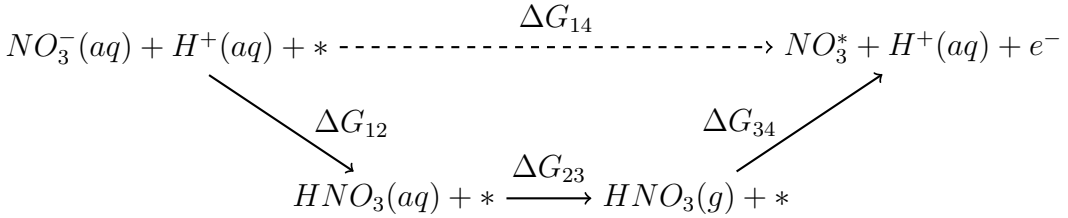

The first reaction step (ΔG_{12}) represents the proton association-dissociation equilibrium of nitric acid, for which the free energy change can be obtained from its pKa (-1.28).[2] Reaction step two (ΔG_{23}) represents the de-solvation process of nitric acid, for which free energy change can be obtained from its Henry's constant ($2100\ \frac{\text{mol}}{\text{m}^3\cdot\text{Pa}}$).[3] At 1 mol/L solution standard state (1 bar, 298 K), ΔG_{12} and ΔG_{23} are 0.08 $\frac{\text{eV}}{\text{V}}$ and 0.40 $\frac{\text{eV}}{\text{V}}$, respectively. For step three (ΔG_{34}), we applied the CHE model to compute $H^+(aq) + e^-$ as $\frac{1}{2}H_2$ at 0.0 V vs SHE and pH=0. Other energies, including gas phase HNO_3 and H_2 as well as the bare slab and slab with NO_3^*, are computed with GC-DFT/DFT and thermochemistry corrections. Hence, to compute the grand free energy of NO_3^- adsorption at any pH and potential, we utilized eq. (S5). Note that we are using $\Phi(U)$ to represent grand free energies and G to represent non-potential dependent free energies.

$$\Delta\Phi_{\text{ads}}^{\text{NO}_3{}^*}(U) = \Phi_{\text{NO}_3{}^*}(U) - \left(\Phi_{\text{slab}}(U) + G_{\text{HNO}_3} - \frac{1}{2}G_{\text{H}_2}\right) - eU - 0.0592\text{pH} + \Delta G_{13} \quad \text{(S5)}$$

DFT Calculations: JDFTx and VASP

VASP

All DFT calculations for both the CHE model and the analytical GC-DFT method were completed using the Vienna Ab Initio Simulation Package (VASP) with the Revised Perdew-Burke-Ernzerhof functional. A plane wave energy cutoff of 544 eV was used for valence electron expansion, while the core electrons were accounted for using the projected augmented wave potentials. Spin-polarized calculations were done for Ni only. We found that Ni_1Cu energetics and system properties did not change with and without spin-polarization. Each structure was modeled using a 3 × 3 × 4 supercell with the top two layers able to relax (along with adsorbates) and the bottom two layers fixed in their lattice coordinates. Pure metal lattice constants were computed and used to generate each slab. For SAAs, a surface atom in the Cu host metal (computed lattice constant: 3.70 Å) was replaced by the dopant atom(s) to simulate the SAA structure. The Brillouin zone was sampled with a 4 × 4 × 1 Monkhorst–Pack k-point grid. Periodic images in the z-direction were separated by a vacuum layer of 15 Å to minimize interactions. All adsorbates and the two topmost slab layers were relaxed by geometry optimization, with forces converged to <0.01 eV/Å. For transition state searches, we used the Climbing Image Nudge Elastic Band method (CI-NEB) with forces converged to <0.05 eV/Å. All transition states were confirmed to have one large imaginary frequency corresponding to the N-O bond dissociation. Enthalpic and entropic thermochemistry corrections for H_2(g), HNO_3(g), adsorbed nitrate in solution, and nitrate dissociation barriers were computed using the rigid rotor harmonic oscillator approximation as implemented in the Atomic Simulation Environment (ASE).[4]

To generate the data for the analytical GC-DFT model in VASP all simulations were converged in both vacuum and solvent, according to the original work of Agrawal et al.[5] Surface normal dipole moments were extracted from converged vacuum simulations within VASP (LDIPOL=.TRUE.). To compute the polarizability, we performed single-point calculations

(starting from the vacuum-optimized structure) under different EFIELD values of 0.0 V to 0.6 V. We then fit a second-order polynomial to the computed energies as a function of the electric field. The polarizability was determined from the coefficient of the second-order term in the best-fit polynomial. Surface normal dipole moments and polarizabilities are included in the accompanying data file located at the GitHub link.

The electrosorption valencies, changes in the surface normal dipole moments, and charge transfer for nitrate adsorption are shown in Table S4. Figure S5 shows the strong correlation between the change in the surface normal dipole moment and the electrosroption valency for NO_3^- adsorption.

Table S4: Electrosorption valencies, changes in surface normal dipole moments, and charge transfer from NO_3^- to the surface upon adsorption on metals and SAAs (units: eV/V, Debey (D), e^-)

	Electrosorption Valency	$\Delta\mu_{NO_3^*}$	$\Delta q_{NO_3^*}$
$Rh_1Cu(111)$	–0.692	0.459	0.712
$Ni_1Cu(111)$	–0.709	0.434	0.688
$Ru_1Cu(111)$	–0.715	0.426	0.732
$Pd_1Cu(111)$	–0.661	0.505	0.633
Cu(111)	–0.692	0.458	0.638
Pd(111)	–0.766	0.380	0.715
Rh(111)	–0.779	0.346	0.785
Ru(0001)	–0.795	0.316	0.764
Ni(111)	–0.775	0.347	0.748
$Rh_1Cu(100)$	–0.663	0.496	0.704
$Ni_1Cu(100)$	–0.660	0.498	0.666
$Ru_1Cu(100)$	–0.691	0.453	0.726
$Pd_1Cu(100)$	–0.598	0.591	0.608
Cu(100)	–0.611	0.557	0.613
Pd(100)	–0.695	0.472	0.689
Rh(100)	–0.782	0.342	0.781
Ni(100)	–0.736	0.397	0.719

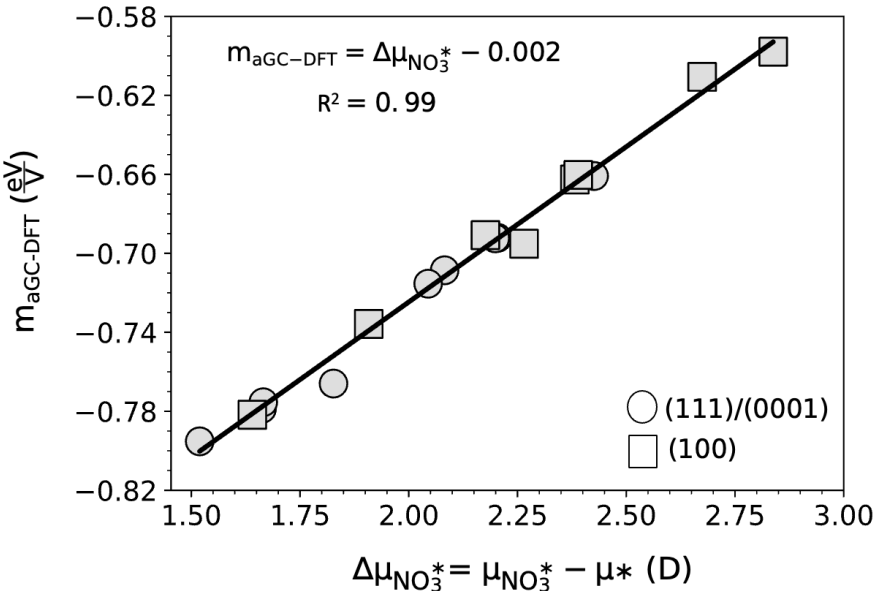

Figure S4: The shift in dipole moment for NO_3^- adsorption versus the electrosorption valency ($m_{aGC\text{-}DFT}$) computed from the analytical GC-DFT method across pure metals and SAAs. The electrosorption valency was computed as the slope of the line-of-best fit to the analytical GC-DFT data.

The symmetry factors, change in the surface normal dipole moments, and charge transfer for nitrate dissociation are shown in Table S5. Figure S5 demonstrates that the charge transfer and change in surface normal dipole moment for nitrate dissociation are poorly correlated.

Table S5: Symmetry factors, changes in surface normal dipole moments, and charge transfer for NO_3* dissociation over metals and SAAs (units: eV/V, Debye (D), unitless)

Metal (facet)	Symmetry Factor	$\Delta\mu_{\ddagger}$	Δq
$Rh_1Cu(111)$	–0.104	–0.743	–0.0411
$Ni_1Cu(111)$	–0.184	–1.324	0.0222
$Ru_1Cu(111)$	–0.109	–0.784	0.0419
$Pd_1Cu(111)$	–0.205	–1.490	0.0346
Cu(111)	–0.175	–1.268	0.0300
Pd(111)	–0.163	–1.152	–0.00941
Rh(111)	–0.168	–1.205	0.0516
Ru(0001)	–0.144	–1.032	0.0293
Ni(111)	-	-	-
$Rh_1Cu(100)$	–0.152	–1.106	–0.0168
$Ni_1Cu(100)$	–0.139	–1.027	–0.0433
$Ru_1Cu(100)$	–0.106	–0.777	0.0226
$Pd_1Cu(100)$	-	-	-
Cu(100)	–0.123	–0.887	–0.118
Pd(100)	–0.152	–1.054	–0.0459
Rh(100)	–0.059	–0.413	–0.0651
Ni(100)	-	-	-

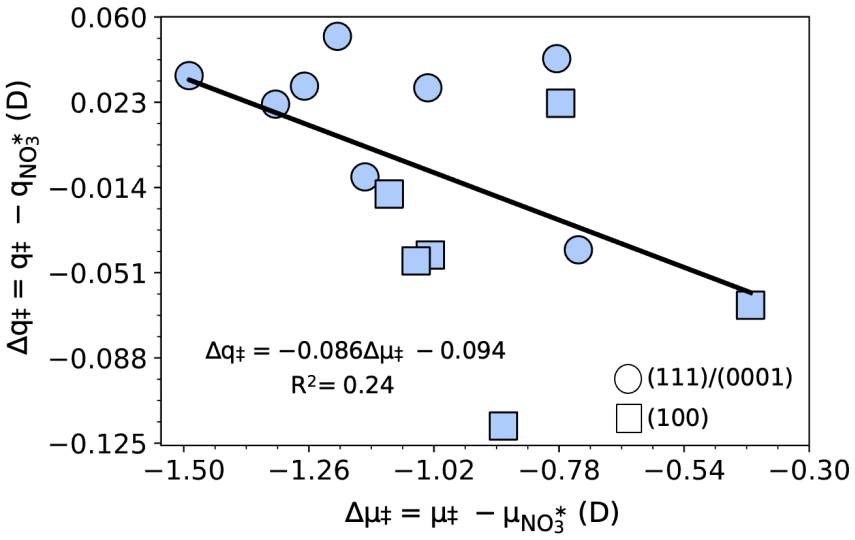

Figure S5: The change in the surface normal dipole moment versus the charge transfer for NO_3^* dissociation, showing a poor correlation between the DFT computed parameters.

JDFTx

All explicit GC-DFT calculations for adsorption and dissociation studies over Cu(111) were completed using the Joint Density Functional Theory Software (JDFTx) with the Revised Perdew-Burke-Ernzerhof Functional. A plane wave energy cutoff of 544 eV was used for valence electron expansion, while the core electrons were accounted for using the projected augmented wave potentials. Cu(111) was modeled using a $3 \times 3 \times 4$ unit cell with 2 relaxed layers with a pure metal lattice constant of 3.70 Å. Refer to section one of the SI for information on computing grand free energies under various potentials and with the CANDLE implicit solvation model. All transition states were confirmed to have one large imaginary frequency corresponding to the N-O bond dissociation. Vibrational frequency calculations were completed in ASE with a JDFTx calculator.[4] Enthalpic and entropic thermochemistry corrections for H_2(g), HNO_3(g), adsorbed nitrate in solution, and nitrate dissociation barriers were computed using the rigid rotor harmonic oscillator approximation as implemented in ASE.[4]

Density of States Calculations

Partial Density of States (pDOS) calculations were performed in VASP using the tetrahedron method (ISMEAR=-5) with an 11×11×1 Gamma-centered k-point grid. Gaussian smoothing was applied to the DOS data to obtain continuous, smooth distributions. The fractional d-band filling was calculated relative to the Fermi level using eq. (S6).

$$f_d = \frac{\int_{-\infty}^{0} \rho(\varepsilon) d\varepsilon}{\int_{-\infty}^{\infty} \rho(\varepsilon) d\varepsilon} \tag{S6}$$

Derivations for the aGC-DFT Model

We start with the most general form of the aGC-DFT model to approximate the change in grand free energy, $\Delta\Phi$, between any two states, χ_1 and χ_2. Shown in eq. S7, n_e represents the number of electrons/protons transferred within a PCET reaction step. We refer the reader to the main text for descriptions of each term within this expression.

$$\begin{aligned}\Delta\Phi(U) = \Delta\Phi(U_{\chi_2}, U_{\chi_1}) - \frac{1}{2}\frac{\varepsilon A}{d}\left((U'_{\chi_2})^2 - (U'_{\chi_1})^2\right) \\ + \mu_{\chi_2}\left(\frac{U'_{\chi_2}}{d}\right) - \mu_{\chi_1}\left(\frac{U'_{\chi_1}}{d}\right) + \frac{\alpha_{\chi_2}}{2}\left(\frac{U'_{\chi_2}}{d}\right)^2 - \frac{\alpha_{\chi_1}}{2}\left(\frac{U'_{\chi_1}}{d}\right)^2 \pm n_e U\end{aligned} \tag{S7}$$

To compute the first-order derivative with respect to the U, we first substitute in $U'_\chi = U - U_\chi$, where $U_\chi = U_0 + \frac{\mu_\chi}{\varepsilon A}$, shown in eq. (S8).

$$\begin{aligned}\Delta\Phi(U) = \Delta\Phi(U_{\chi_2}, U_{\chi_1}) + \frac{2\Delta\mu}{d}(U - U_0) - \frac{3}{2\varepsilon A d}(\mu_{\chi_2}^2 - \mu_{\chi_1}^2) \\ + \frac{\alpha_{\chi_2}\mu_{\chi_2}^2 - \alpha_{\chi_1}\mu_{\chi_1}^2}{2(\varepsilon A d)^2} - \frac{\alpha_{\chi_2}\mu_{\chi_2} - \alpha_{\chi_1}\mu_{\chi_1}}{\varepsilon A d^2}(U - U_0) - \frac{\Delta\alpha}{2d^2}(U - U_0)^2 \pm U n_e\end{aligned} \tag{S8}$$

We then take the deritive of eq. (S8) with respect to U, shown in eq (S9). We write the derivative in this format to demonstrate that negligible polarizability effects yield a linear

potential dependence as a function of $\Delta\mu$.

$$\frac{\partial \Delta\Phi(U)}{\partial U} = \frac{2\Delta\mu}{d} + \frac{\alpha_{\chi_2}}{d^2}\left(U - U_0 - \frac{\mu_{\chi_2}}{\varepsilon A}\right) - \frac{\alpha_{\chi_1}}{d^2}\left(U - U_0 - \frac{\mu_{\chi_1}}{\varepsilon A}\right) \pm n_e \tag{S9}$$

The electrosorption valency for the NO_3^* adsorption ($\chi_1 = *, \chi_2 = NO_3^*$) is derived by observing that $\alpha_* = 0$ and $n_e = -1.0$. Additionally, the symmetry factor for NO_3^* dissociation ($\chi_1 = NO_3^*$, $\chi_2 = \ddagger$) is derived by setting $n_e = 0$ because there is no PCET during the dissociation.

We also use eq. (S8) to derive an expression for the error in neglecting EDL effects for both NO_3^* adsorption and NO_3^* dissociation, shown in eq. (S10). The first term in the error expression indicates the capacitive energy to charge the double layer, and the second term accounts for dipole-field interactions. For derivation purposes, we neglect polarizability effects in deriving eq. (S10). However, the errors presented in-text are computed with polarizability effects, albeit small.

$$\Sigma_{ABS} \approx \left|\frac{2\Delta\mu}{d}(U - U_0) - \frac{3}{2\varepsilon A d}(\mu_{\chi_2}^2 - \mu_{\chi_1}^2)\right| \tag{S10}$$

Rewriting eq. (S10) as eq. (S11) because $\Sigma_{ABS} = \Sigma_{SQ}$, we can compute the potential at which the error is minimized, $U_{\min}$, by taking the derivative of eq. (S11) and setting it to zero. The full expression is shown in eq. (S12)

$$\Sigma_{SQ} \approx \sqrt{\left(\frac{2\Delta\mu}{d}(U - U_0) - \frac{3}{2\varepsilon A d}(\mu_{\chi_2}^2 - \mu_{\chi_1}^2)|\right)^2} \tag{S11}$$

$$U_{min} \approx U_0 + \frac{3}{4\varepsilon A}(\mu_{\chi_1} + \mu_{\chi_2}) \tag{S12}$$

References

(1) Darby, M. T.; Sykes, E. C. H.; Michaelides, A.; Stamatakis, M. Carbon Monoxide Poisoning Resistance and Structural Stability of Single Atom Alloys. *Topics in Catalysis* **2018**, *61*, 428–438.

(2) Lange, N. A. *Lange's handbook of chemistry*, 16th ed.; McGraw-Hill standard handbooks; McGraw-Hill Education: New York, 2013.

(3) Sander, R. Compilation of Henry's law constants (version 4.0) for water as solvent. *Atmospheric Chemistry and Physics* **2015**, *15*, 4399–4981.

(4) Hjorth Larsen, A. et al. The atomic simulation environment—a Python library for working with atoms. *Journal of Physics: Condensed Matter* **2017**, *29*, 273002.

(5) Agrawal, N.; Wong, A. J.-W.; Maheshwari, S.; Janik, M. J. An efficient approach to compartmentalize double layer effects on kinetics of interfacial proton-electron transfer reactions. *Journal of Catalysis* **2024**, *430*, 115360.